1-1-2016

Breakaway oxidation behaviour of ferritic stainless steels at 1150 °C in humid air

Xiawei Cheng
University of Wollongong, xiawei@uow.edu.au

Zhengyi Jiang
University of Wollongong, jiang@uow.edu.au

Brian J. Monaghan
University of Wollongong, monaghan@uow.edu.au

Dongbin Wei
University of Wollongong, dwei@uow.edu.au

Raymond Longbottom
University of Wollongong, rayl@uow.edu.au

See next page for additional authors

Breakaway oxidation behaviour of ferritic stainless steels at 1150 °C in humid air

Abstract

The breakaway oxidation behaviour of ferritic stainless steels 430, 443 and 445 has been investigatedat 1150◦C in humid air. The oxidation kinetics exhibited significant differences among the three ferriticstainless steels. A uniform and steady growing oxide scale was developed on the 430 steel with an evensteel/oxide interface. Local breakdown of the initially protective oxide scale occurred and oxide noduleswere developed on the 443 and 445 stainless steels, resulting in irregular and rough steel/oxide inter-faces. The breakaway oxidation behaviour was significantly influenced by the microstructure and thecomposition of the oxide scale. The Mn-Cr spinel oxide formed on top of the Cr2O3scale in Mo alloying445 steel can greatly minimise the Cr depletion.

Keywords

air, humid, c, 1150, oxidation, steels, breakaway, stainless, ferritic, behaviour

Disciplines

Engineering | Science and Technology Studies

Publication Details

Cheng, X., Jiang, Z., Monaghan, B. J., Wei, D., Longbottom, R. J., Zhao, J., Peng, J., Luo, M., Ma, L., Luo, S. & Jiang, L. (2016). Breakaway oxidation behaviour of ferritic stainless steels at 1150 °C in humid air. Corrosion Science, 108 11-22.

Authors

Xiawei Cheng, Zhengyi Jiang, Brian J. Monaghan, Dongbin Wei, Raymond Longbottom, Jingwei Zhao, Jianguo Peng, Ming Luo, Li Ma, Suzhen Luo, and Laizhu Jiang

Breakaway oxidation behaviour of ferritic stainless steels at 1150 °C in humid air

Xiawei Cheng[1], Zhengyi Jiang[1,*], Brian J. Monaghan[1], Dongbin Wei[1,2], Raymond J. Longbottom[1], Jingwei Zhao[1], Jianguo Peng[3], Ming Luo[3], Li Ma[3], Shuzheng Luo[3], Laizhu Jiang[3]

[1]School of Mechanical, Materials and Mechatronic Engineering, University of Wollongong, NSW 2522, Australia
[2]School of Electrical, Mechanical and Mechatronic Systems, University of Technology Sydney, NSW 2007, Australia
[3]Baosteel Research Institute (R&D Centre), Baoshan Iron & Steel Co., Ltd., Shanghai 200431, PR China

Abstract

The breakaway oxidation behaviour of ferritic stainless steels 430, 443 and 445 has been investigated at 1150 °C in humid air. The oxidation kinetics exhibited significant differences among the three ferritic stainless steels. A uniform and steady growing oxide scale was developed on the 430 steel with an even steel/oxide interface. Local breakdown of the initially protective oxide scale occurred and oxide nodules were developed on the 443 and 445 stainless steels, resulting in irregular and rough steel/oxide interfaces. The breakaway oxidation behaviour was significantly influenced by the microstructure and the composition of the oxide scale. The Mn-Cr spinel oxide formed on top of the Cr_2O_3 scale in Mo alloying 445 steel can greatly minimise the Cr depletion.

Keywords: Ferritic stainless steel; High temperature oxidation; Water vapour; Oxide scale; Reheating

* Corresponding author. Tel: +61-2-42214545; Fax: +61-2-42215474

E-mail addresses: xiawei@uow.edu.au (X. Cheng), jiang@uow.edu.au (Z. Jiang)

1. Introduction

Ferritic stainless steels without nickel appear to be a promising candidate material for use in solid oxide fuel cell (SOFC) stacks and automobile exhaust pipes. They are cheap and have a lower thermal expansion coefficient than that of austenitic steels [1], which is clearly an advantage when the temperature cycling resistance is needed. Ferritic stainless steels have a body-centred-cubic (bcc) crystal structure, which is beneficial to Cr diffusion in the steel matrix [2]. The start of the breakaway oxidation of the stainless steel leads to a period of more rapid oxidation at elevated temperature and indicates the failure of the protective chromia scale and the formation of non-protective iron-rich oxide scale. The oxidation temperature, the oxygen partial pressure, the oxidation time, the water vapour content of the atmosphere and the Cr content of the alloy all have significant effects on breakaway oxidation [2-5]. The oxidation rate increases with increasing oxygen partial pressure and decreasing chromium concentration [6]. The oxidation rate in the wet gas is three to five orders of magnitude higher than that in the dry gas [7]. Long-term oxidation of ferritic stainless steels has been extensively investigated at temperature ranges below 1000 °C [8-11], in which the breakaway oxidation might take place but the process is slow due to the relatively slow chemical reaction and the low solid-state diffusion rates [12].

A large amount of Cr_2O_3 evaporation will occur in a mixed atmosphere of O_2 and H_2O. Cr_2O_3 evaporates linearly with time, depending on the concentration of O_2 and H_2O vapour [13, 14] [15-18]. Asteman et al. [12, 19-21] showed that Cr vaporization between 600 and 900 °C can lead to a depletion of Cr in the outer oxide scales of austenitic steels and to the formation of fast-growing Fe-rich oxides at high air-flow rates. Continuous evaporation eventually causes the loss of chromia, if its growth

cannot be maintained by the supply of Cr from the underlying steel, or the overall Cr level underneath the oxide scale reaches a level below the required concentration. This will cause the formation of poorly protective Fe-rich oxide scale and thus an increased oxidation rate [19, 22].

In hot rolling, stainless steel slabs are placed in a reheating furnace at a temperature up to 1250 °C where the atmosphere generally contains moisture due to the natural gas combustion and/or humid conditions. In most stainless steel grades, breakaway oxidation and the Cr depletion occurs during the heating process [23-25]. The oxidation behaviour of stainless steels during reheating plays a role in their deformation behaviour during the process of hot rolling [26, 27]. The aim of the present paper is to analyse the breakaway oxidation behaviour of three commercial ferritic stainless steels in the presence of $H_2O+O_2+N_2$ at 1150 °C. Three different breakaway oxidation behaviours occurred. Investigation into oxidation kinetics, microstructure and composition of the oxide scales was carried out.

2. Experimental method

2.1. Materials

Three ferritic stainless steel grades, 430, 443 and 445, were investigated in this study. Their chemical compositions are given in Table 1. Samples were tempered for 5 min at 980 °C and then machined to a size of 20 × 10 × 1 mm^3 with a small hole of 2 mm in diameter near one edge. Prior to the oxidation experiments, all the samples were ground on all sides with 1200 grit SiC sandpaper, then cleaned in acetone and rinsed with alcohol. Stainless steel 430 was chemically etched in Villella's etchant [28] (picric acid 1 g + hydrochloric acid 10 ml + ethanol 100 ml) and 443 and 445 steels were electrolytically etched in 10% aqueous oxalic acid at 15 V for 60 s. The

microstructures of the ferritic stainless steels are shown in Fig. 1. The optical micrographs in Fig. 1 show that the grain size of the 430 steel was 114±45 μm without counting recrystallised grains, while the grain size of the 443 steel was 81±73 μm, which was smaller than the grain size of the 445 steel, 98±80 μm.

2.2. Oxidation experiments

The oxidation kinetics of stainless steels was investigated using a thermogravimetric analyser (TGA). The temperature of the steel sample was calibrated by attaching a Type-R thermocouple to a representative sample. Samples were put in a vertical tube furnace and isothermally heated for 7200 s. The mass change of a sample during the TGA experiment was measured using a Sartorius CP124S microbalance with a resolution of 10^{-4} g, and a computer recorded the value automatically. A simulated humid atmosphere with 18% water vapour was generated by bubbling 1000 ml/min of synthetic air through a water bath heated to 58.4 °C. The gas inlet line was heated to prevent water vapour condensation. The total gas pressure was 1 atm.

The furnace was heated to 1150 °C at a heating rate of 20 °C/min, and then humid air was made to flow through the furnace. The furnace was held at the set temperature for 30 minutes, then the steel sample was lowered into the hot zone of the furnace and the weight change logged. After the set time of 7200 s, the experiment was ended by removing the sample from the furnace and cooling it to room temperature.

2.3. Analysis of oxide scale

Oxide scales formed on the samples were surface scanned using X-ray diffraction (XRD) for phase identification. After surface analysis, all the samples were cold

mounted in epoxy resin, then sectioned and polished. The microstructures, compositions and thickness of the oxide scale were examined by a JEOL JSM 6490 scanning electron microscope (SEM) equipped with an energy dispersive spectrometer (EDS). Back-scattered electrons (BSE) were employed for imaging the steel/oxide interface. A KEYENCE 3D laser-scanning microscope examined the etched oxidised samples.

3. Results

3.1. Oxidation kinetics in humid air

The isothermal oxidation kinetics, represented by the mass-gain curve vs. time for the stainless steel specimens oxidised at 1150 °C for 7200 s in humid air containing 18% water vapour are presented in Fig. 2a. Fig. 2b shows the parabolic plot of mass gain squared as a function of time, while Fig. 2c shows the incubation period to the onset of breakaway oxidation from Fig. 2b in more detail. Fig. 2a shows that for the 430 and the 443 steel samples, the oxidation rate had an obvious abrupt increase. For the 445 steel, the increase in the oxidation rate was much less and no abrupt increase in oxidation was observed during the experiment. The initial period of oxidation can be indicated by the time required for a mass gain of 1 mg/cm^2. As shown in Fig. 2c, it took approximately 300 s for the 443 and the 445 steels to obtain a mass gain of 1 mg/cm^2, indicating that the initial period of oxidation of the 443 and the 445 steels is similar. For the 430 steel, 160 s was required to achieve the same gain in mass.

Compliance to the parabolic law indicates that the reaction is of a diffusion-controlled character [29]. High temperature oxidation kinetics of metals or alloys is commonly controlled by the diffusion of cationic or anionic species through the oxide scale [30].

Such a control leads to a parabolic rate constant, k_p expressed in $mg^{2}\cdot cm^{-4}\cdot s^{-1}$, and defined by [30]:

$$(\Delta m/s)^2 = A + k_p t \quad (1)$$

where $\Delta m/s$ is the specific mass gain per area unit in mg/cm^2, t is the oxidation time, and A is a constant. Table 2 shows the parabolic rate constants before and after breakaway oxidation for the ferritic stainless steels in humid air. R^2 was used to quantify the fit of the model to the data. k_p values and associated R^2 values were calculated for fits of Eq. (1) to the data in Fig. 2b. The parabolic growth rate constant k_p values of the 443 and the 445 steels are 3.75×10^{-3} and 3.91×10^{-3} $mg^{2}\cdot cm^{-4}\cdot s^{-1}$, respectively, using the initial time of 300 s. A significant difference, however, took place after 600 s. The iron oxides or oxide nodules were developed at this stage, in which the k_p value of the 443 steel was 191 times greater than that of the 445 steel.

3.2 Oxide scale microstructure

The surface morphology of the oxide scale formed on three ferritic stainless steels oxidised for 7200 s in humid air is presented in Fig. 3a-c. No oxide scale spallation was observed. On the 430 steel, the oxide scale appeared thick, even and homogeneous. On the 443 steel, the thick oxide scale covered a majority of the surface but there were still some small regions having a thin oxide scale. On the 445 steel, the oxidised surface was very coarse and localised oxide nodules appeared either merged or isolated. Fig. 3d-f shows the cross section of oxide scale for the corresponding steels. On the 430 steel, an even surface and steel/oxide interface was observed and the thickness fraction of iron oxides to Fe-Cr spinel was roughly 1:1. On

the 443 steel, an irregular and wavy steel/oxide interface was observed. The thickness fraction of iron oxides was less than that of the Fe-Cr spinel where there was a multi-layer oxide scale. On the 445 steel, a very rough and irregular steel/oxide interface was observed. Fe-Cr spinel formed underneath the original Cr_2O_3 scale.

Fig. 4 is the results of a scan of the surfaces showing the XRD patterns of the oxidised stainless steel specimens. XRD analysis revealed that the surface layers of oxide scale of the 430 and the 443 steels were mainly Fe_2O_3, but the 430 steel showed a higher intensity. On the 445 steel, Cr_2O_3, Fe_2O_3 and spinel M_3O_4 were detected. M might be Cr, Mn, and/or Fe because of the similar ionic radii of Cr, Mn, and Fe [4]. The spinel may not have stoichiometric compositions as diffraction peaks shift slightly to the lower angle. The spinel oxides might contain alloying elements Cr, Fe, Mn, Nb, and Mo. With the aid of EDS spot, line and map element analysis on the cross section of the oxide scale, the composition of the spinel was identified.

3.3 Steel/oxide interface of the multi-layer oxide scale

The Fe-Cr spinel oxides with a higher Cr content appear darker in the images. Fig. 5 shows the BSE image and EDS element maps of the cross section of steel/oxide interface on the 430 steel. Table 3 shows the chemical compositions of the points identified in Fig. 5 as measured by EDS quantitative analysis. Internal Cr enriched oxides were formed. The oxides have a $(Fe_{1-x}Cr_x)_3O_4$ spinel structure. The paler oxides were found to contain more Fe than Cr, but the darker Fe-Cr spinel oxides have roughly a 1:1 atom ratio of Fe to Cr. The interfacial concentration of Cr, where the spectrum 1 is located, is 8.8 wt. %. This is only half the amount of Cr in the steel substrate. Si is distributed randomly in the oxides but appears more where there is a

high intensity of Cr.

Fig. 6 shows the BSE image and EDS element maps of the cross section of the steel/oxide interface on the 443 steel. Internal Cr enriched oxides were observed to be like tree roots. Table 4 shows the chemical compositions of the points identified in Fig. 6 as measured by EDS quantitative analysis. The oxides mainly consist of a $(Fe_{1-x}Cr_x)_3O_4$ spinel structure. The paler oxides were found to contain more Fe than Cr. The darker Fe-Cr spinel oxides have roughly an atomic ratio of Fe to Cr of 1:1.5. The interfacial concentration of Cr, where the spectrum 1 is located, is 7.9 wt. %. This is far less than the amount of Cr in the steel substrate. Si is distributed more at the steel/oxide interface and at the site where the internal oxides are.

Fig. 7 shows the BSE image and EDS element maps of the cross section of the steel/oxide interface on the 445 steel. Table 5 shows the chemical compositions of the points identified in Fig. 7 as measured by EDS quantitative analysis. Internal Si enriched oxides were observed, which were discontinuous at the steel/oxide interface. The spinel oxide appeared darker than that on the 430 and 443 steels. At the steel/oxide interface, the oxide structure is Cr_2O_3 with a thickness of 4.3±0.9 μm. The interfacial concentration of Cr, where spectrum 1 is located is 20.5 wt. %. This is nearly the same amount of Cr in the steel substrate, indicating that there is no Cr depletion at the steel/oxide interface. Mo is also found having 1.0 wt.% at the steel/oxide interface, which is higher than the amount of Mo in the steel substrate.

4. Discussion

Three stainless steel grades 430, 443 and 445 displayed different breakaway oxidation behaviour at 1150 ˚C in humid air. 430 steel has a Cr content of 16.20 wt.%, which is less than the other two grades. Si and Mn are present in the 430 steel, but they had little effect on the oxidation behaviour because breakaway oxidation took place quickly at 1150 ˚C. Saeki et al. [31-33] have intensively studied the initial oxidation of 430 stainless steel. Cheng et al.[34] have investigated the oxidation kinetics of 430 stainless steel at high temperature. They concluded that the chemical failure model best described the oxide change during breakaway oxidation. This mechanism of chemical failure is caused by a chromium concentration gradient across the specimen section to a level below that needed to generate a healing chromia layer [35]. There was more Fe-enriched spinel $(Fe_{1-x}Cr_x)_3O_4$ in the oxidised 430 sample (Fig. 5), which was beneficial for Fe cations to migrate outwards [29]. Compared with the 430 steel, the 443 and 445 steels had longer incubation times. Ferritic stainless steel 445 has shown high oxidation resistance in the reheating environment before hot rolling [36]. The breakaway oxidation phenomenon of the 445 steel, however, was significantly different from that of the 443 steel (Fig. 2). The mass change curve of the 443 steel showed an abrupt increase in the oxide scale growth rate when the chromia transits to iron oxides. The slow oxide growth rate of the 445 steel may be attributed to the regeneration of the Cr_2O_3 underneath the iron oxide (Fig. 7). This is referred as a "healing" layer [37] . The interfacial chromium activity is high to stabilise Cr_2O_3.

BSE examination was carried out on the cross-section of the thin oxide scale where the oxide nodules had not grown on the 443 steel. The steel grains can be seen in Fig.

8a. They became large during oxidation in the experiment. The grain size was 228±146 μm. Fig. 8b shows the cross-section of oxidised 443 steel. The EDS element maps and Fig.9 show a very strong intensity of Cr in the oxide scale, indicating that the thin oxide scale constituted mainly of Cr_2O_3. Si was accumulated at the steel/oxide interface, but the silica layer was porous and discontinuous. The oxide was a corundum structure M_2O_3 at the oxide/gas interface. The oxide scale was 7.3±1.1 μm thick and this oxide scale was less adherent to the steel substrate because large voids existed at the steel/oxide interface. Nb appears at the top of the oxide scale along with very small amounts of Mn, Ti and Fe. Internal Ti-enriched oxides were formed in the subscale.

BSE examination was carried out on the cross-section of the thin oxide scale where the oxide nodules have not grown on the 445 steel. The steel grains can be seen in Fig. 10a. They became large during oxidation just like those in the 443 steel, and the grain size was 272±170 μm. Fig. 10b shows the cross-section of oxidised 445 steel. The EDS element maps and Fig. 11 show a very strong intensity of Cr in the oxide scale, indicating a thin oxide scale mainly constituted of Cr_2O_3. Si accumulated at the steel/oxide interface, and the silica layer was still discontinuous. The oxide scale was 8.8±0.9 μm thick and this oxide scale was thicker and exhibited better adherence to the steel substrate than that on the 443 steel. The voids at the steel/oxide interface of the 445 steel were smaller than those of the 443 steel. The oxide was a spinel structure M_3O_4 at the oxide/gas interface. Mo, Nb, Fe and Ti appeared on the top of the oxide scale. Mn had very strong intensity on the top and was present in the thin oxide scale. The spinel was mainly $(Mn, Cr)_3O_4$ doped with a small amount of the alloying elements Mo, Nb, Fe and Ti. Internal Ti-enriched oxides were formed in the subscale.

An interesting phenomenon of the oxidised 445 sample is shown in Fig. 10c, where the oxide nodules appeared more on the flat surface but less on the edges. It is commonly accepted that extra stresses are generated within the oxide scale grown near the edges of the specimen, so oxide scale cracks will tend to be formed near or on the edges, and this will result in breakaway oxidation, and Fe-enriched oxide nodules will appear more in these regions [29, 38, 39]. The explanation for this phenomenon is that there is not much Cr depletion in this steel during oxidation, even underneath the Cr_2O_3 scale having a mechanical failure.

In order to develop and maintain the Cr_2O_3 scale, the interfacial concentration of Cr, $N_{Cr}^{(i)}$, is determined by the rates at which Cr is being consumed by the Cr_2O_3 scale growth and replenished by Cr diffusion in the alloy. Wagner's diffusion analysis [40] leads to [41]:

$$N_{Cr}^{(i)} = N_{Cr}^{(0)} - \frac{V_A}{V_{CrO_{1.5}}}\left(\frac{\pi k_c}{2\widetilde{D}}\right)^{1/2} \quad (2)$$

$N_{Cr}^{(0)}$ is the original alloy chromium concentration. There is only a small difference in the amount of Cr in the 443 and the 445 steels. V_A and $V_{CrO_{1.5}}$ are the molar volumes of alloy and oxide scale, respectively, $\widetilde{D}$ is the alloy interdiffusion coefficient, and k_c is the parabolic rate constant for growth of the external scale that is measured in terms of the oxide scale thickness.

k_c can also be calculated from k_p, the parabolic rate constant from mass gain, using M_aO_b for an oxide film which can be expressed as [30]:

$$k_c = \left(\frac{\Delta M \times M_{ox}}{S b M_o \rho_{ox}}\right)^2 k_p \quad (3)$$

where ΔM is the mass gain, S is the surface area, M_{ox} is the molar mass of the oxide, M_o is the molar mass of the oxygen atom, ρ_{ox} is the volumic mass of the oxide. In our study, M_aO_b is Cr_2O_3 so that b=3. From Table 2, the formation of Cr_2O_3 of the 443 and the 445 steels has similar k_p values at the initial stage.

$\widetilde{D}$, the diffusion coefficient of Cr in the alloy, can be calculated by:

$$\widetilde{D} = (1 - f)D_L + fD_{GB} \quad (4)$$

where D_L is a summation of lattice diffusivity and D_{GB} is grain boundaries diffusion of Cr in the metal. f is the area proportion of grain boundary. If the grains are cubic, then $f = 2\delta/d$ (δ is the grain boundary width and d the grain size). By considering $D_{GB} >> D_L$, Eq. (4) can be simplified as:

$$\widetilde{D} = D_L + \frac{2\delta}{d} D_{GB} \quad (5)$$

Hence, $\widetilde{D}$ increases with decreasing d. The 443 and 445 stainless steels have roughly the same steel structures (Fig. 1). The remaining Cr_2O_3 scale on the 445 steel (Fig. 9b) is thicker than that on the 443 steel (Fig. 8b). The growth of the Cr_2O_3 scale on the 445 steel will not cause more Cr depletion than that on the 443 steel. Moreover, from the experimental results, Cr is preserved soundly in 445 steel. The growth of the Cr_2O_3 scale at the initial stage is obviously not the reason to cause severe depletion of

Cr in the 443 steel. The oxidation atmosphere and the composition of the oxide scale need to be considered.

It is well known that the oxidation behaviour of alloys in environments that contain water vapour differs strongly from that in 'dry' atmospheres e.g. oxygen or air. However, there is still not a complete understanding of the mechanism behind these observations. Generally, the exposure of Fe-Cr alloys to O_2/H_2O mixtures can result in Cr depletion of the protective oxide by evaporation of chromium species by the following reactions [3, 19, 29, 39, 42-44]:

$$Cr_2O_3\,(s) + 3/2\,O_2\,(g) = 2\,CrO_3\,(g) \quad (6)$$

$$1/2Cr_2O_3\,(s) + H_2O\,(g) + 3/4O_2\,(g) = CrO_2\,(OH)_2\,(g) \quad (7)$$

In oxygen-water vapour atmospheres, chromium (VI) oxo-hydroxide $CrO_2(OH)_2$ exhibits much higher partial pressure than CrO_3 [45]. The content of water vapour in air, at which the transition from CrO_3 to $CrO_2(OH)_2$ occurs at 850 °C, was determined by Gindorf et al. [46, 47].

Then, the equilibrium partial pressure of the volatile oxy-hydroxide is given by:

$$P_{CrO_2(OH)_2}\,(g) = KP_{H_2O}(g) \cdot P_{O_2}{}^{3/4}\,(g) \quad (8)$$

where K, the equilibrium constant, is given by:

$$\ln(K) = B/T + C \quad (9)$$

Here B and C are constants. The calculated equilibrium constants according to the thermodynamic databases in Ebbinghaus [48], Stanislowski et al. [49], Opila et al. [50], and Gindorf et al. [47], are shown in Fig. 12. The data of the equilibrium vaporization experiments was derived from pure Cr_2O_3(s) but when the Cr_2O_3 scale formed on alloys had an outer layer of well-adhered $(Mn, Cr)_3O_4$ spinel, Al_2O_3 or Co_3O_4, the Cr vaporization rates were greatly reduced [49].

Our study was carried out in humid air with 18% water vapour at 1 atm. The partial pressure for O_2 and H_2O is 0.164 and 0.18 atm, respectively. The value of K is high at 1150 °C so volatile Cr species will form at such an atmosphere. The high oxide growth rate of the 443 steel is in accordance with this phenomenon after the incubation period. This is caused by the Cr depletion in the subscale zone [29, 51]. Generally, the greater the extent of the Cr depletion, the less likely it will be for the Cr_2O_3 scale to be healed or reformed [35, 52]. This is not applicable, however, to the oxidation behavior of the 445 steel (Fig. 2). The regenerated Cr_2O_3 (Fig. 7) was formed and a discontinuous network of silica particles were present at and beneath the steel/oxide interface (Fig. 7). Bamba et al. [53] found that the latter phenomenon impedes the counter flow of Cr vacancies to the bulk of the steel by providing sinks, thus reducing the flux of Cr atoms entering the scale. On the 445 steel, a continuous and compact $(Mn,Cr)_3O_4$ spinel layer doped with a small amount of alloying elements Mo, Nb, Fe and Ti on top of the Cr_2O_3 scale (Fig.9) may help prevent Cr evaporation. However, Nb, Fe and Ti were also present on top of the Cr_2O_3 scale on the 443 steel, therefore an effect of Nb, Fe and Ti on Cr evaporation seems unlikely. Mo was

present in the Mn-Cr spinel, and it showed intensity at steel/oxide interface (Table 2) without depletion. Many researchers have found that Mn-Cr spinel can strongly reduce $CrO_2(OH)_2$ volatilisation when it is present at the external interface [54-58].

Sachitanand et al. [59] and Stanislowski et al. [60] showed that the Cr vaporization of chromia-forming steels can be reduced by more than 90% by alloying. Stainless steels containing Mn 0.3–0.5 wt.% develop a well adherent $(Cr,Mn)_3O_4$ spinel top layer above the Cr_2O_3-layer at 800 and 850 °C, and that the rate of Cr vaporization for those alloys is 2–3 times lower than alloys that form pure Cr_2O_3 scales or a non-continuous $(Mn,Cr)_3O_4$ top layer.

The build-up of oxide scale on alloys is determined by thermodynamics and kinetics [29]. Thermodynamics, particularly the Gibbs free energy of formation of oxides, plays the major role in selective oxidation. Huttunen-Saarivirta et al. [61] found that the elements of Ti, Si, Nb and Mo were related to the oxidation performance of alloys with Cr content >11.5 wt. %. The alloy elements are preferentially oxidised in an order: Ti >Si>Nb>Mn>Cr>Fe>Mo [39, 61] . Humid air in our study is an atmosphere located in a high oxygen partial pressure region, which is high enough to form various oxides. For the ferritic stainless steels, the amount of the alloying element, e.g. Ti, Si, Nb, Mn, Mo, is minor. TiO_2 and $(Mn,Cr)_3O_4$ were found on the outer side of the Cr_2O_3 layer, and SiO_2 was located below the Cr_2O_3 layer in different atmospheres [6, 24, 61-67]. In a Fe-based alloy containing Cr as a solute, an outer layer of Cr oxide Cr_2O_3 will preferentially form during the early stages of oxidation prior to the formation of any Fe oxides. At elevated temperature, however, Fe ions will dissolve in and diffuse rapidly through the Cr_2O_3 scale and eventually an outer layer of Fe

oxides will result although Fe thermodynamically has much less affinity for O_2 than Cr [68]. Water vapour accelerates oxide nodule nucleation and growth [37, 69]. The phase stability and oxidation behavior of the Fe-Cr-O ternary system were assessed using thermodynamic calculation [29, 39] [70, 71]. Fe-Cr alloys with changing compositions exist in equilibrium with different oxides at increasing oxygen pressure. Considering the Cr content of ferritic stainless steels is around 20 wt.%, at the high oxygen partial pressure region at the oxide surface, the phase stability predicts Fe_2O_3. In the intermediate oxygen partial pressure region, several oxides may present, including Fe_3O_4, FeO, and $FeCr_2O_4$ spinel. At the low oxygen partial pressure region at the steel/oxide interface, the Fe-Cr alloy exists in equilibrium with a corundum phase, which is almost identical to Cr_2O_3 [38, 72]. Thermodynamic calculations suggest that higher Cr content results in an oxide with a higher fraction of corundum $(Cr, Fe)_2O_3$ compared to the spinel $(Fe,Cr)_3O_4$ phase. The difference in Cr concentration may affect not only the fraction of oxides formed, but also the ratio of Cr/Fe in each phase [70], which is in agreement with our study (Fig.3).

During oxidation, the Cr depletion of the 443 steel below the Cr_2O_3 scale prevailed in the sample due to the volatile Cr species, and this resulted in the formation of more and more Fe-rich oxide nodules and overall Cr loss in the steel. A thick and banded scale occurred (Figs. 3 and 6), and the oxidation rate was accelerated by alternating external and internal oxidation [18]. Töpfer et al. [73] showed that the Fe tracer diffusion coefficient was about 3 orders of magnitude higher than that of Cr over a range of oxygen activity in $(Fe,Cr)_3O_4$ spinels at 1200 °C. It has also been seen that the spinel at the steel/oxide interface at low oxygen partial pressure region is not stable at 1150 °C. More and more localised Fe-rich nodules formed and spread

quickly and this can account for the high oxidation rate of the 443 steel after breakaway oxidation.

In our study, the largest difference in the alloying elements between the 445 and the 443 steels are Mn and Mo, although the Mn content in the 445 steel is only 0.15 wt.%. These two alloying elements, however, can affect the composition of the oxide scale and cause significant difference in breakaway oxidation of the two steels at 1150 °C in humid air. Because negligible Mn was in the oxide scale of the 443 steel at the end of the test, the amount of Mn at the top of the oxide film was limited by the small amount of Mn in the steel [74]. Mo is added to steels mainly to enhance their mechanical properties and can slightly improve their oxidation resistance at moderate amount but its effect varies with the amount of Cr content and the test environment [75]. The addition of 0.1–2 wt.% Mo reduces the oxidation rate of the Fe–22Cr–0.5Mn steel [76], but more than 4 wt.% Mo added can cause the evaporation of volatile Mo species which reduces the stability of the protective chromia, resulting in a high oxidation rate. Long term passivation in wet air was achieved by adding 2.2 wt.% Mo to 9Cr-3W ferritic steel [77]. Yun et al. [76] found that Mo addition did not have a significant effect on the evaporation of Cr at 800 °C. Mo can be concentrated at the steel/oxide interface or a Mo -rich second phase may form at the steel/oxide interface and the metal grain boundary, and thus improve adhesion of the Cr_2O_3 scale to the steel [76, 78, 79].

Our study showed distinct silica particles forming along and accumulating at the oxide/metal interface (Figs. 8 and 10) before breakaway oxidation on the 443 and the 445 steels. On the 445 steel, underneath the oxide nodule a discontinuous network of

silica particles reappeared but this characterisation of Si only existed when there was no Cr depletion (Fig. 7) in the steel. This phenomenon did not take place in the 430 or the 443 steels with similar amounts of Si (Figs. 5 and 6).

5. Conclusions

The isothermal oxidation behaviour of ferritic stainless steel grades 430, 443 and 445 was studied at 1150 °C in humid air. The breakaway oxidation of three steels took place quickly (430 and 443 steels) or slowly (445 steel) during the test time.

1. Multi-layer oxide scale formed on the 430 steel showed a uniform thickness and an even steel/oxide interface due to the complete Cr depletion in the steel.

2. $(Fe, Cr)_3O_4$ with different ratios of Fe to Cr from steel to steel was found in the multi-layer oxide scale with a spinel structure.

3. Grain sizes of the three stainless steels had little effect on their oxidation behaviour at 1150 °C in the experiment.

4. Oxide nodules did not appear more on or near the edges of the 445 steel because of less Cr depletion in this steel.

5. The extent of Cr depletion in the steel affects the breakaway oxidation behaviour of two similar stainless steels 443 and 445. The alloying elements Mn and Mo in the 445 steel have effects on the composition and microstructure of the oxide scale. The formation of compact and continuous Mn-Cr spinel on top of the

Cr_2O_3 scale on Mo alloying 445 steel greatly reduce the evaporation of chromium species.

Acknowledgements

The authors acknowledge the Baosteel-Australia Joint Research and Development Centre financial support for the current project under Grant number BA11017. The authors would like to acknowledge the use of facilities within the University of Wollongong (UOW) Electron Microscopy Centre. The authors wish to gratefully acknowledge the help of Dr. Madeleine Strong Cincotta from the University of Wollongong in the final language editing of this paper.

References

[1] M. Cortie, Ferritic Stainless Steels, in: Encyclopedia of Materials: Science and Technology (second ed), Elsevier, Oxford, 2001, pp. 3037-3039.
[2] A.M. Huntz, A. Reckmann, C. Haut, C. Severac, M. Herbst, F.C.T. Resende, A.C.S. Sabioni, Oxidation of AISI 304 and AISI 439 stainless steels, Mater. Sci. Eng. A, 447 (2007) 266-276.
[3] J. Shen, L. Zhou, T. Li, High-temperaute oxidation of Fe-Cr alloys in wet oxygen, Oxid. Met., 48 (1997) 347-356.
[4] Z. Yang, G. Xia, P. Singh, J.W. Stevenson, Effects of water vapor on oxidation behavior of ferritic stainless steels under solid oxide fuel cell interconnect exposure conditions, Solid State Ionics, 176 (2005) 1495-1503.
[5] A.N. Hansson, M. Montgomery, m.A.J. Somers, Oxidation of X20 in water vapour: the effedt of temperature and oxygen partial pressure, Oxid Met, 71 (2009) 201-218.
[6] M. Palcut, L. Mikkelsen, K. Neufeld, M. Chen, R. Knibbe, P.V. Hendriksen, Corrosion stability of ferritic stainless steels for solid oxide electrolyser cell interconnects, Corros. Sci., 52 (2010) 3309-3320.
[7] J. Ehlers, D.J. Young, E.J. Smaardijk, A.K. Tyagi, H.J. Penkalla, L. Singheiser, W.J. Quadakkers, Enhanced oxidation of the 9%Cr steel P91 in water vapour containing environments, Corros. Sci., 48 (2006) 3428-3454.
[8] C. Issartel, H. Buscail, Y. Wang, R. Rolland, M. Vilasi, L. Aranda, Water vapour effect on ferritic 4509 steel oxidation between 800 and 1000 °C, Oxid Met, 76 (2011) 127-147.
[9] A.L. Marasco, D.J. Young, The oxidation of iron-chromium-manganese alloys at 900°C, Oxid. Met., 36 (1991) 157-174.

[10] B. Pujilaksono, T. Jonsson, H. Heidari, M. Halvarsson, J.-E. Svensson, L.-G. Johansson, Oxidation of binary FeCr alloys (Fe–2.25Cr, Fe–10Cr, Fe–18Cr and Fe–25Cr) in O2 and in O2 + H2O environment at 600 °C, Oxid Met, 75 (2011) 183-207.
[11] J. Rufner, P. Gannon, P. White, M. Deibert, S. Teintze, R. Smith, H. Chen, Oxidation behavior of stainless steel 430 and 441 at 800 °C in single (air/air) and dual atmosphere (air/hydrogen) exposures, Int. J. Hydrogen Energy, 33 (2008) 1392-1398.
[12] H. Asteman, J.E. Svensson, L.G. Johansson, Evidence for Chromium Evaporation Influencing the Oxidation of 304L: The Effect of Temperature and Flow Rate, Oxid. Met., 57 (2002) 193-216.
[13] A. Yamauchi, K. Kurokawa, H. Takahashi, Evaporation of Cr_2O_3 in atmospheres containing H_2O, Oxid. Met., 59 (2003) 517-527.
[14] J. Żurek, M. Michalik, F. Schmitz, T.U. Kern, L. Singheiser, W.J. Quadakkers, The Effect of Water-Vapor Content and Gas Flow Rate on the Oxidation Mechanism of a 10%Cr-Ferritic Steel in Ar-H2O Mixtures, Oxid. Met., 63 (2005) 401-422.
[15] D. Huenert, A. Kranzmann, Impact of oxyfuel atmospheres H2O/CO2/O2 and H2O/CO2 on the oxidation of ferritic-martensitic and austenitic steels, Corros. Sci., 53 (2011) 2306-2317.
[16] M.P. Brady, M. Fayek, J.R. Keiser, H.M. Meyer, K.L. More, L.M. Anovitz, D.J. Wesolowski, D.R. Cole, Wet oxidation of stainless steels: New insights into hydrogen ingress, Corros. Sci., 53 (2011) 1633-1638.
[17] L. Martinelli, C. Desgranges, F. Rouillard, K. Ginestar, M. Tabarant, K. Rousseau, Comparative oxidation behaviour of Fe-9Cr steel in CO2 and H2O at 550 °C: Detailed analysis of the inner oxide layer, Corrosion Science, 100 (2015) 253-266.
[18] T. Jonsson, B. Pujilaksono, H. Heidari, F. Liu, J.E. Svensson, M. Halvarsson, L.G. Johansson, Oxidation of Fe–10Cr in O2 and in O2 + H2O environment at 600 °C: A microstructural investigation, Corros. Sci., 75 (2013) 326-336.
[19] H. Asteman, J.E. Svensson, L.G. Johansson, Oxidation of 310 steel in H2O/O2 mixtures at 600 °C: the effect of water-vapour-enhanced chromium evaporation, Corros. Sci., 44 (2002) 2635-2649.
[20] H. Asteman, J.E. Svensson, L.G. Johansson, M. Norell, Indication of Chromium Oxide Hydroxide Evaporation During Oxidation of 304L at 873 K in the Presence of 10% Water Vapor, Oxid. Met., 52 (1999) 95-111.
[21] H. Asteman, J.E. Svensson, M. Norell, L.G. Johansson, Influence of Water Vapor and Flow Rate on the High-Temperature Oxidation of 304L; Effect of Chromium Oxide Hydroxide Evaporation, Oxid. Met., 54 (2000) 11-26.
[22] M. Halvarsson, J.E. Tang, H. Asteman, J.E. Svensson, L.G. Johansson, Microstructural investigation of the breakdown of the protective oxide scale on a 304 steel in the presence of oxygen and water vapour at 600 °C, Corros. Sci., 48 (2006) 2014-2035.
[23] L.-F. Li, Z.-H. Jiang, Y. Riquier, High-temperature oxidation of duplex stainless steels in air and mixed gas of air and CH4, Corros. Sci., 47 (2005) 57-68.
[24] Q. Jin, J. Li, Y. Xu, X. Xiao, W. Zhang, L. Jiang, High-temperature oxidation of duplex stainless steels S32101 and S32304 in air and simulated industrial reheating atmosphere, Corros. Sci., 52 (2010) 2846-2854.
[25] S.Y. Cheng, S.L. Kuan, W.T. Tsai, Effect of water vapor on annealing scale formation on 316 SS, Corros. Sci., 48 (2006) 634-649.

[26] X. Cheng, Z. Jiang, J. Zhao, D. Wei, L. Hao, J. Peng, M. Luo, L. Ma, S. Luo, L. Jiang, Investigation of oxide scale on ferritic stainless steel B445J1M and its tribological effect in hot rolling, Wear, 338–339 (2015) 178-188.
[27] X. Cheng, Z. Jiang, D. Wei, L. Hao, J. Zhao, L. Jiang, Oxide scale characterization of ferritic stainless steel and its deformation and friction in hot rolling, Tribol. Int., 84 (2015) 61-70.
[28] D.J. Ha, C.-Y. Son, J.W. Park, J.S. Lee, Y.D. Lee, S. Lee, Effects of high-temperature hardness and oxidation on sticking phenomena occurring during hot rolling of two 430J1L ferritic stainless steels, Mater. Sci. Eng. A, 492 (2008) 49-59.
[29] D.J. Young, High Temperature Oxidation And Corrosion Of Metals, Elsevier, Oxford, 2008.
[30] A.M. Huntz, Parabolic laws during high temperature oxidation: relations with the grain size and thickness of the oxide, J. Mater. Sci. Lett., 18 (1999) 1981-1984.
[31] I. Saeki, H. Konno, R. Furuichi, The initial oxidation of type 430 stainless steel in O2□H2O□N2 atmospheres at 1273 K, Corros. Sci., 38 (1996) 19-31.
[32] I. Saeki, Y. Sugiyama, S. Hayashi, A. Yamauchi, T. Doi, Y. Nishiyama, S. Kyo, S. Suzuki, M. Sato, S. Fujimoto, In situ X-ray diffraction of surface oxide on type 430 stainless steel in breakaway condition using synchrotron radiation, Corros. Sci., 55 (2012) 219-225.
[33] I. Saeki, H. Konno, R. Furuichi, T. Nakamura, K. Mabuchi, M. Itoh, The effect of the oxidation atmosphere on the initial oxidation of type 430 stainless steel at 1273 K, Corros. Sci., 40 (1998) 191-200.
[34] X. Cheng, Z. Jiang, D. Wei, J. Zhao, B.J. Monaghan, R.J. Longbottom, L. Jiang, High temperature oxidation behaviour of ferritic stainless steel SUS 430 in humid air, Met. Mater. Int., 21 (2015) 251-259.
[35] H.E. Evans, Mechanisms of breakaway oxidation and application to a chromia forming steel, Oxid. Met., 52 (1999) 379-401.
[36] X. Cheng, Z. Jiang, D. Wei, J. Zhao, B.J. Monaghan, R.J. Longbottom, L. Jiang, Characteristics of oxide scale formed on ferritic stainless steels in simulated reheating atmosphere, Surf. Coat. Technol., 258 (2014) 257-267.
[37] T. Gheno, D. Monceau, D.J. Young, Mechanism of breakaway oxidation of Fe-Cr and Fe-Cr-Ni alloys in dry and wet carbon dioxide, Corros. Sci., 64 (2012) 222-233.
[38] L. Mikkelsen, High Temperature Oxidation of Iron-Chromium Alloys, in: Riso National Laboratory, Southern Denmark, Roskilde, 2003, pp. 173.
[39] N. Birks, G.H. Meier, F.S. Pettit, High-Temperature Oxidation of Metals, 2nd ed., Cambridge University Press, Cambridge, 2005.
[40] C. Wagner, Theoretical analysis of the diffusion processes determining the oxidation rate of alloys, J. Electrochem. Soc., 99 (1952) 369-380.
[41] N.K. Othman, N. Othman, J. Zhang, D.J. Young, Effects of water vapour on isothermal oxidation of chromia-forming alloys in Ar/O2 and Ar/H2 atmospheres, Corrosion Science, 51 (2009) 3039-3049.
[42] Oxidation, in.
[43] A. Fry, S. Osgerby, M. Wright, Oxidation of alloys in steam environments-A Review, in, NPL Materials Centre, Middlesex, UK, 2002.
[44] S. Mrowec, An Introduction to the Theory of Metal Oxidation, National Center for Scientific, Technical and Economic Information, 1982.
[45] K. Segerdahl, J.E. Svensson, M. Halvarsson, I. Panas, L.G. Johansson, Breakdown of the protective oxide on 11% Cr steel at high temperature in the

presence of water vapor and oxygen, the influence of chromium vaporization, Mater. High Temp., 22 (2005) 69-78.
[46] C. Gindorf, L. Singheiser, K. Hilpert, Vaporisation of chromia in humid air, J. Phys. Chem. Solids, 66 (2005) 384-387.
[47] C. Gindorf, L. Singheiser, K. Hilpert, Chromium vaporisation from Fe,Cr base alloys used as interconnect in fuel cells, Steel Res. Int., 72 (2001) 528-533.
[48] B.B. Ebbinghaus, Thermodynamics of gas phase chromium species: The chromium oxides, the chromium oxyhydroxides, and volatility calculations in waste incineration processes, Combust. Flame, 93 (1993) 119-137.
[49] M. Stanislowski, E. Wessel, K. Hilpert, T. Markus, L. Singheiser, Chromium Vaporization from High-Temperature Alloys, J. Electrochem. Soc., 154 (2007) A295-A306.
[50] E.J. Opila, N.S. Jacobson, D.L. Myers, E.H. Copland, Predicting oxide stability in high-temperature water vapor, JOM, 58 (2006) 22-28.
[51] W. Pavlichko, J.H. Hoke, Precipitates, Intergranular attack and Cr depletion in ferritic stainless steel, Microstr. Sc., 4 (1976) 3-12.
[52] S. Henry, A. Galerie, L. Antoni, Abnormal oxidation of stabilized ferritic stainless steels in water vapor, Mater. Sci. Forum, 369-372 (2001) 353-360.
[53] G. Bamba, Y. Wouters, A. Galerie, F. Charlot, A. Dellali, Thermal oxidation kinetics and oxide scale adhesion of Fe–15Cr alloys as a function of their silicon content, Acta Mater., 54 (2006) 3917-3922.
[54] Z.G. Yang, G.G. Xia, J.W. Stevenson, Mn1.5Co1.5O4 spinel protection layers on ferritic stainless steels for SOFC interconnect applications, Electrochem. Solid-State Lett., 8 (2005) A168-A170.
[55] Z.G. Yang, J.S. Hardy, M.S. Walker, G.G. Xia, S.P. Simner, J.W. Stevenson, Structure and conductivity of thermally grown scales on ferritic Fe-Cr-Mn steel for SOFC interconnect applications, J. Electrochem. Soc., 151 (2004) A1825-A1831.
[56] S.P. Simner, M.D. Anderson, G.G. Xia, Z. Yang, L.R. Pederson, J.W. Stevenson, SOFC performance with Fe-Cr-Mn alloy interconnect, J. Electrochem. Soc., 152 (2005) A740-A745.
[57] G.R. Holcomb, D.E. Alman, The effect of manganese additions on the reactive evaporation of chromium in Ni–Cr alloys, Scripta Mater., 54 (2006) 1821-1825.
[58] H. Li, W. Chen, High temperature carburization behaviour of Mn–Cr–O spinel oxides with varied concentrations of manganese, Corros. Sci., 53 (2011) 2097-2105.
[59] M.P. Brady, J.R. Keiser, K.L. More, M. Fayek, L.R. Walker, R.A. Peascoe-Meisner, L.M. Anovitz, D.J. Wesolowski, D.R. Cole, Comparison of short-term oxidation behavior of model and commercial chromia-forming ferritic stainless steels in dry and wet air, Oxid. Met., 78 (2012) 1-16.
[60] M. Stanislowski, J. Froitzheim, L. Niewolak, W.J. Quadakkers, K. Hilpert, T. Markus, L. Singheiser, Reduction of chromium vaporization from SOFC interconnectors by highly effective coatings, J. Power Sources, 164 (2007) 578-589.
[61] E. Huttunen-Saarivirta, V.T. Kuokkala, P. Pohjanne, Thermally grown oxide films and corrosion performance of ferritic stainless steels under simulated exhaust gas condensate conditions, Corros. Sci., 87 (2014) 344-365.
[62] A. Yamauchi, Y. Suzuki, N. Sakaguchi, S. Watanabe, S. Taniguchi, K. Kurokawa, Microstructure and analysis of oxide scales formed on Cr–Si–Ni compacts in air and H2O-containing atmosphere, Corros. Sci., 52 (2010) 2098-2103.
[63] C. Yu, T.D. Nguyen, J.Q. Zhang, D.J. Young, Corrosion of Fe-9Cr-(Mn, Si) alloys in CO2-H2O-SO2 gases, Corros. Sci., 98 (2015) 516-529.

[64] T.D. Nguyen, J.Q. Zhang, D.J. Young, Effects of cerium and manganese on corrosion of Fe-Cr and Fe-Cr-Ni alloys in Ar-20CO(2) and Ar-20CO(2)-20H(2)O gases at 650 degrees C, Corros. Sci., 100 (2015) 448-465.
[65] T.D. Nguyen, J.Q. Zhang, D.J. Young, Water vapour effects on corrosion of Fe-Cr and Fe-Cr-Ni alloys containing cerium and manganese in CO2 gas at 818 degrees C, Corros. Sci., 89 (2014) 220-235.
[66] H. Li, Y. Zheng, L.W. Benum, M. Oballa, W. Chen, Carburization behaviour of Mn–Cr–O spinel in high temperature hydrocarbon cracking environment, Corros. Sci., 51 (2009) 2336-2341.
[67] X. Montero, F. Tietz, D. Stöver, M. Cassir, I. Villarreal, Evaluation of commercial alloys as cathode current collector for metal-supported tubular solid oxide fuel cells, Corros. Sci., 51 (2009) 110-118.
[68] G.H. Meier, K. Jung, N. Mu, N.M. Yanar, F.S. Pettit, J.P. Abellan, T. Olszewski, L.N. Hierro, W.J. Quadakkers, G.R. Holcomb, Effect of Alloy Composition and Exposure Conditions on the Selective Oxidation Behavior of Ferritic Fe–Cr and Fe–Cr–X Alloys, Oxid. Met., 74 (2010) 319-340.
[69] T. Gheno, D. Monceau, D.J. Young, Kinetics of breakaway oxidation of Fe-Cr and Fe-Cr-Ni alloys in dry and wet carbon dioxide, Corros. Sci., 77 (2013) 246-256.
[70] V.S. Dheeradhada, H. Cao, M.J. Alinger, Oxidation of ferritic stainless steel interconnects: Thermodynamic and kinetic assessment, J. Power Sources, 196 (2011) 1975-1982.
[71] L. Kjellqvist, M. Selleby, B. Sundman, Thermodynamic modelling of the Cr–Fe–Ni–O system, Calphad, 32 (2008) 577-592.
[72] J.R. Taylor, A.T. Dinsdale, Thermodynamic assessment of the Cr-Fe-O system, Zeitschrift fuer Metallkunde/Materials Research and Advanced Techniques, 84 (1993) 335-345.
[73] J. Töpfer, S. Aggarwal, R. Dieckmann, Point defects and cation tracer diffusion in (CrxFe1 - x)3 - δO4 spinels, Solid State Ionics, 81 (1995) 251-266.
[74] M. Reichardt, Surface oxide formation and acid-descaling for stainless steel, Wire Ind., 68 (2001) 503, 505-507.
[75] V. Lepingle, G. Louis, D. Allué, B. Lefebvre, B. Vandenberghe, Steam oxidation resistance of new 12%Cr steels: Comparison with some other ferritic steels, Corros. Sci., 50 (2008) 1011-1019.
[76] D.W. Yun, H.S. Seo, J.H. Jun, J.M. Lee, K.Y. Kim, Molybdenum effect on oxidation resistance and electric conduction of ferritic stainless steel for SOFC interconnect, Int. J. Hydrogen Energy, 37 (2012) 10328-10336.
[77] S. Tang, S. Zhu, X. Tang, H. Pan, Z.D. Xiang, Effects of Co, Al and Mo on the long term passivation of 9Cr-3W (wt.%) ferritic steels in air and wet air at 650 degrees C, Corros. Sci., 82 (2014) 255-264.
[78] A. Safikhani, M. Esmailian, M.R. Salmani, M. Aminfard, Effect of Ni-Mo addition on cyclic and isothermal oxidation resistance and electrical behavior of ferritic stainless steel for SOFCs interconnect, Int. J. Hydrogen Energy, 39 (2014) 11210-11223.
[79] H. Buscail, S. El Messki, F. Riffard, S. Perrier, R. Cueff, E. Caudron, C. Issartel, Characterization of the oxides formed at 1000 degrees C on the AISI 316L stainless steel - Role of molybdenum, Mater. Chem. Phys., 111 (2008) 491-496.

Table captions

Table 1 Chemical compositions of ferritic stainless steels 430, 443 and 445 (wt.%).

Table 2 k_p values obtained at 1150 °C for three ferritic stainless steels oxidised in humid air.

Table 3 EDS quantitative analysis data of spectra in Fig. 5 (at. %) of the 430 steel oxidised for 7200 s at 1150 °C in humid air.

Table 4 EDS quantitative analysis data of spectra in Fig. 6 (at. %) of the 443 steel oxidised for 7200 s at 1150 °C in humid air.

Table 5 EDS quantitative analysis data of spectra in Fig. 7 (at. %) of the 445 steel oxidised for 7200 s at 1150 °C in humid air.

Figure captions

Fig. 1 Optical micrograph of etched ferritic stainless steel samples (a) 430, (b) 443, and (c) 445.

Fig. 2 Oxidation kinetics of three ferritic stainless steels in humid air. (a) $\Delta m/s$–t plots, (b) $(\Delta m/s)^2$ –t plots, and (c) $(\Delta m/s)^2$ –t plots during the initial stage.

Fig. 3 SEM micrographs of the oxidised surfaces oxidised for 7200 s at 1150 °C in humid air: (a) 430, (b) 443, (c) 445 and BSE micrographs of the cross sections of the oxide scales (d) 430, (e) 443, and (f) 445.

Fig. 4 XRD patterns of the surface scan after the steels oxidised for 7200 s at 1150 °C in humid air.

Fig. 5 The BSE micrograph of the cross section of steel/oxide interface and EDS element maps of 430 steel oxidised for 7200 s at 1150 °C in humid air.

Fig. 6 The BSE micrograph of the cross section of steel/oxide interface and EDS element maps of 443 steel oxidised for 7200 s at 1150 °C in humid air.

Fig. 7 The BSE micrograph of the cross section of steel/oxide interface and EDS element maps of 445 steel oxidised for 7200 s at 1150 °C in humid air.

Fig. 8 (a) Optical micrograph of the cross section showing steel grains of oxidised 443 steel, and (b) the BSE micrograph of the cross section of thin oxide scale and EDS element maps of 443 steel oxidised for 7200 s at 1150 °C in humid air.

Fig. 9 The result of a EDS linescan along A-B in Fig.8b of thin oxide scale formed on 443 steel oxidised for 7200 s at 1150 °C in humid air. The oxide was a corundum structure M_2O_3 at the oxide/gas interface.

Fig. 10 (a) Optical micrograph of the cross section showing steel grains of oxidised 445 steel, (b) the BSE micrograph of the cross section of thin oxide scale and EDS

element maps of 445 steel, and (c) image of oxidised surface of 445 steel oxidised for 7200 s at 1150 °C in humid air.

Fig. 11 The result of a EDS linescan along A-B in Fig.10b of the thin oxide scale formed on 445 steel oxidised for 7200 s at 1150 °C in humid air. The oxide was a spinel structure M_3O_4 at the oxide/gas interface.

Fig. 12 Equilibrium constant K as a function of the inverse temperature for the reaction $1/2Cr_2O_3$ (s) + H_2O (g) + $3/4O_2$ (g) = CrO_2 $(OH)_2$ (g) according to in Ebbinghaus [48], Stanislowski et al. [49], Opila et al. [50], and Gindorf et al. [47]. Pure Cr_2O_3 was used for the reaction.

Table 1 Chemical compositions of ferritic stainless steels 430, 443 and 445 (wt.%).

	C	Si	Mn	P	Cr	Cu	Mo	Ti	Nb
430	0.04	0.30	0.40	<0.02	16.20	0.03	0.00	<0.01	<0.01
443	≤0.01	0.35	<0.10	0.00	21.00	0.40	0.00	0.14	0.20
445	≤0.01	0.30	0.15	0.03	21.50	0.10	0.60	≤0.20	0.12

Table 2 k_p values obtained at 1150 °C for three ferritic stainless steels oxidised in humid air

Steel grades	**k_p values ($mg^2 \cdot cm^{-4} \cdot s^{-1}$)**	**R^2**
430 (before 100 s)	Cannot be obtained	
430 (after 300 s)	1.69	0.99
443 (before 300 s)	3.75×10^{-3}	0.80
443 (after 600 s)	6.40×10^{-1}	0.99
445 (before 300 s)	3.91×10^{-3}	0.81
445 (after 600 s)	3.35×10^{-3}	0.97

Table 3 EDS quantitative analysis data of spectra in Fig. 5 (at. %) of the 430 steel oxidised for 7200 s at 1150 °C in humid air

Spectrum	Cr	Fe	O	Si	P
1	9.4	90.6			
2	21.5	19.5	57.0	1.8	0.2
3	5.5	38.9	55.1	0.5	
4	17.5	18.0	59.9	3.9	0.7

Table 4 EDS quantitative analysis data of spectra in Fig. 6 (at. %) of the 443 steel oxidised for 7200 s at 1150 °C in humid air

Spectrum	Cr	Fe	O	Si	Cu
1	8.4	90.4			1.2
2	25.4	16.7	57.4	0.5	
3	4.3	44.8	50.4	0.5	
4	25.5	17.2	55.7	1.6	

Table 5 EDS quantitative analysis data of spectra in Fig. 7 (at. %) of the 445 steel oxidised for 7200 s at 1150 °C in humid air

Spectrum	Cr	Fe	O	Si	Cu	Mo	Ti	Nb
1	21.7	76.6		0.6	0.5	0.6		
2	34.9	1.3	62.2	0.3			1.3	
3	13.9	24.6	61.2				0.3	
4	9.6	27.3	41.9	21.2				
5	8.6	10.6	56.3				24.3	0.2

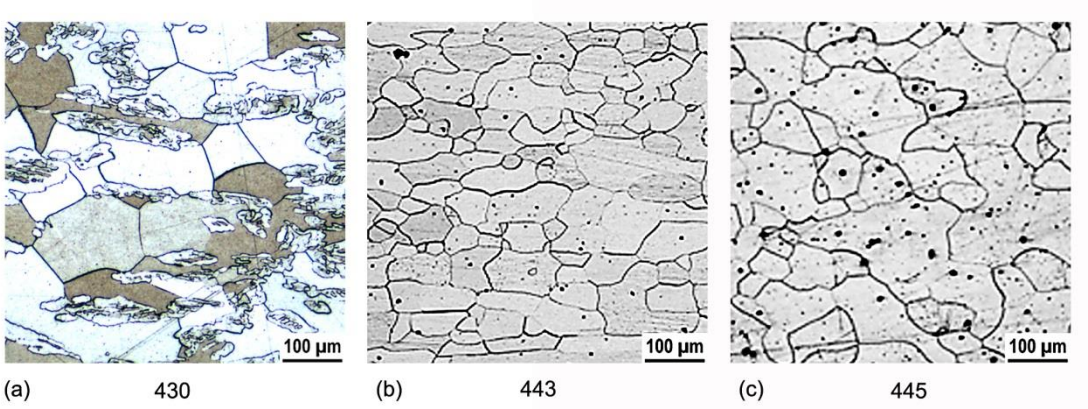

Fig. 1 Optical micrograph of etched ferritic stainless steel samples: (a) 430, (b) 443, and (c) 445.

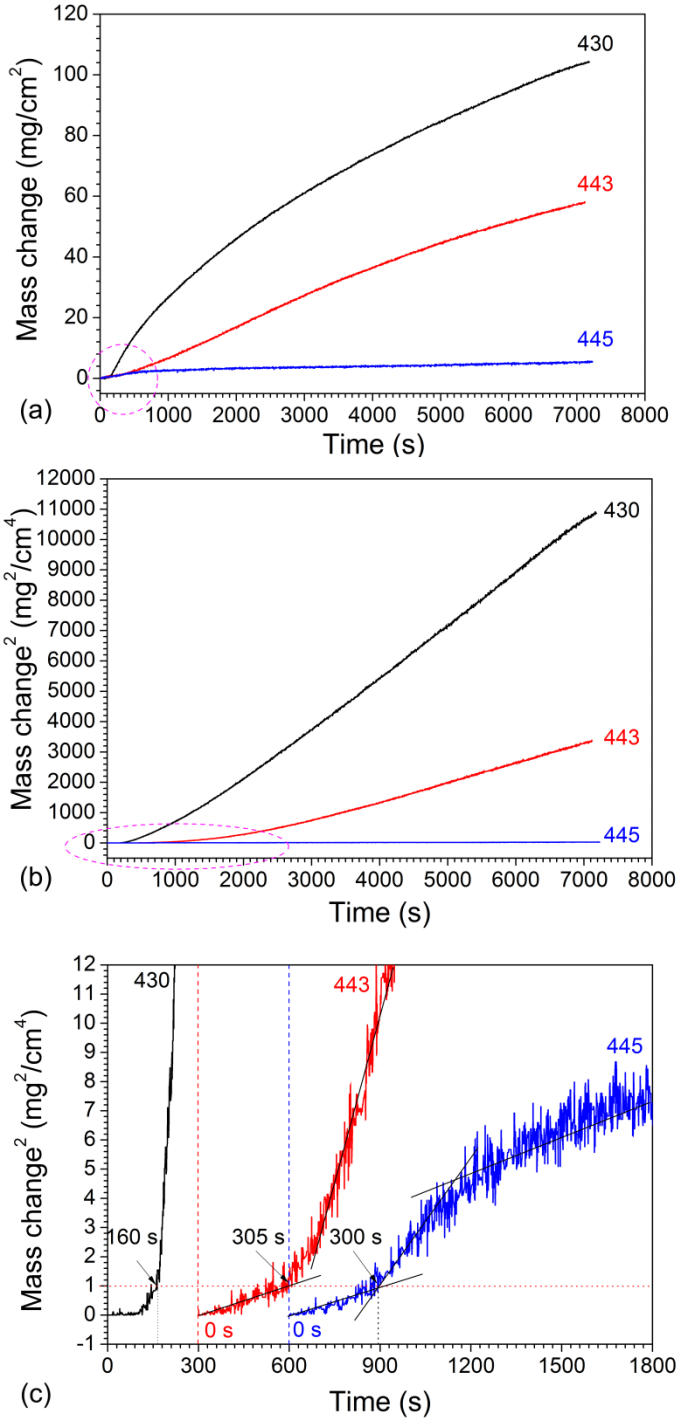

Fig. 2 Oxidation kinetics of three ferritic stainless steels in humid air. (a) $\Delta m/s$–t plots, (b) $(\Delta m/s)^2$ –t plots, and (c) $(\Delta m/s)^2$ –t plots during the initial stage.

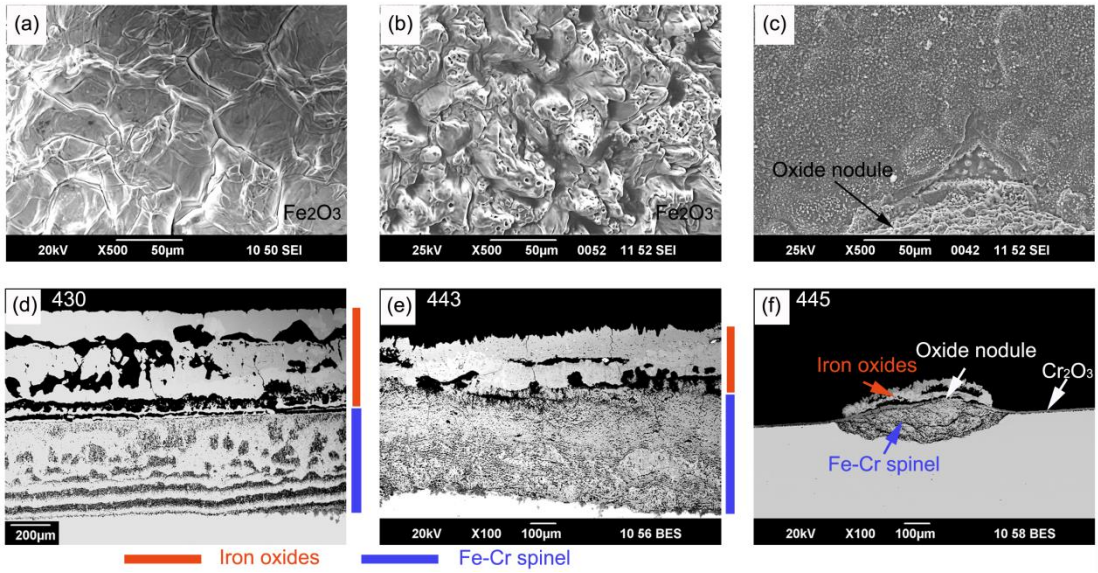

Fig. 3 SEM micrographs of the oxidised surfaces oxidised for 7200 s at 1150 °C in humid air: (a) 430, (b) 443, (c) 445 and BSE micrographs of the cross sections of the oxide scales (d) 430, (e) 443, and (f) 445.

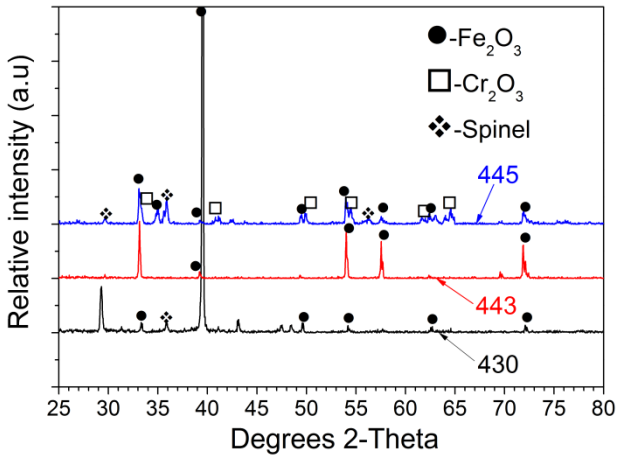

Fig. 4 XRD patterns of the surface scan after the steels oxidised for 7200 s at 1150 °C in humid air.

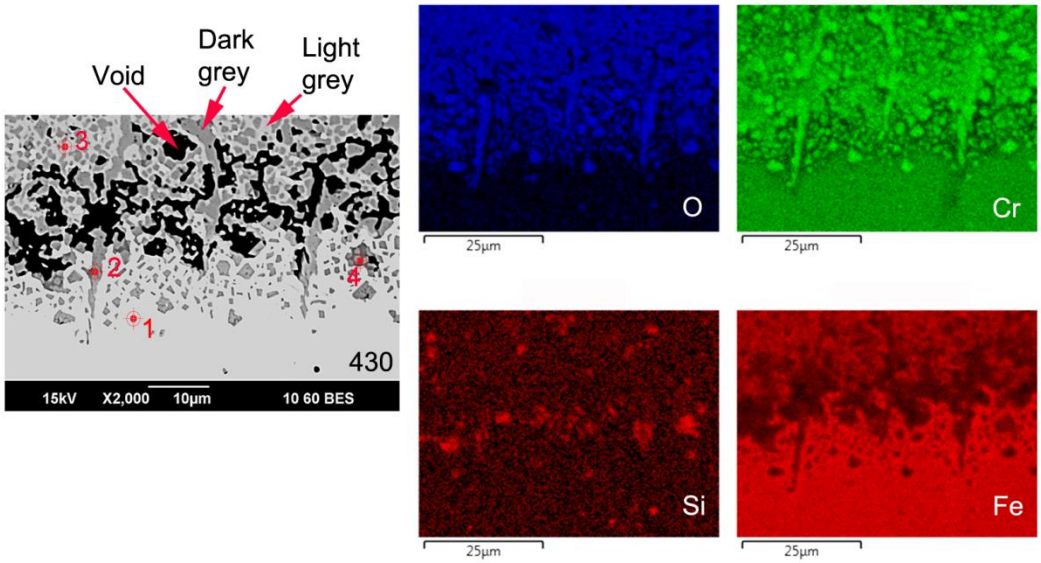

Fig. 5 The BSE micrograph of the cross section of steel/oxide interface and EDS element maps of 430 steel oxidised for 7200 s at 1150 °C in humid air.

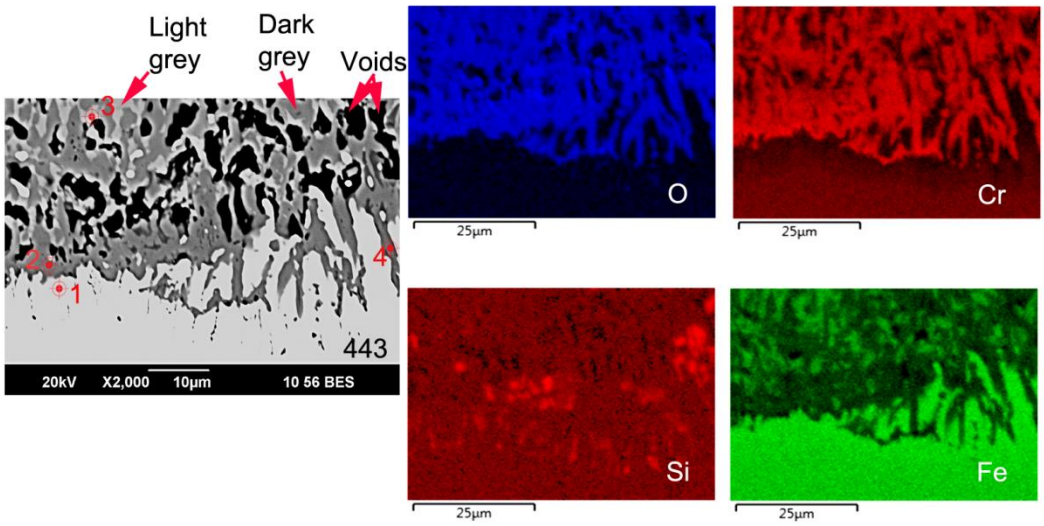

Fig. 6 The BSE micrograph of the cross section of steel/oxide interface and EDS element maps of 443 steel oxidised for 7200 s at 1150 °C in humid air.

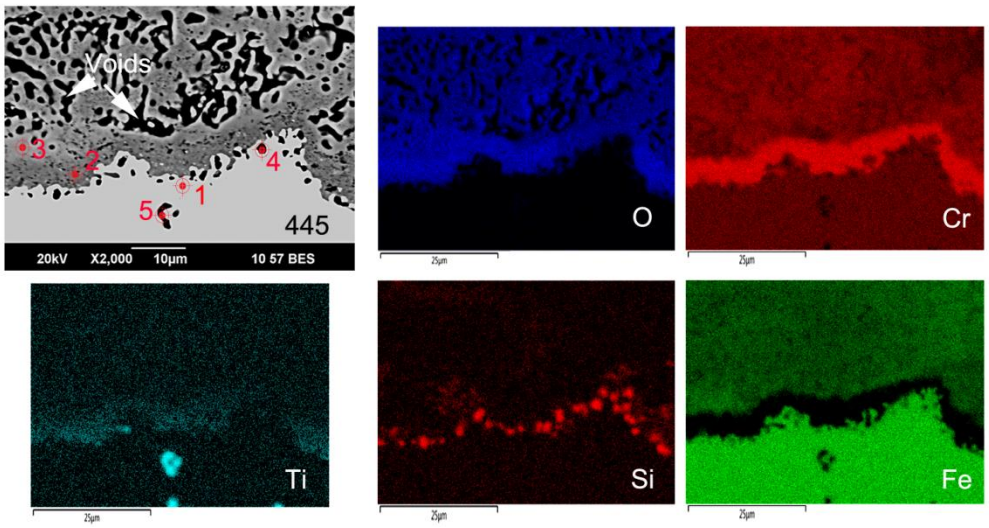

Fig. 7 The BSE micrograph of the cross section of steel/oxide interface and EDS element maps of 445 steel oxidised for 7200 s at 1150 °C in humid air.

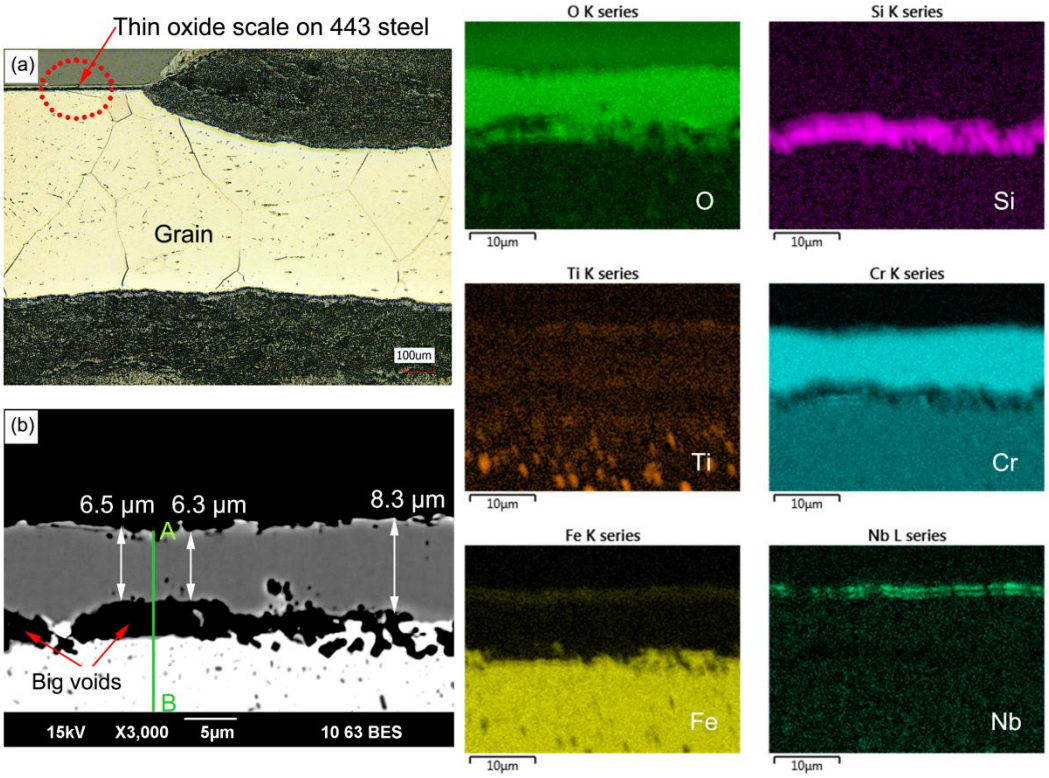

Fig. 8 (a) Optical micrograph of the cross section showing steel grains of oxidised 443 steel, and (b) the BSE micrograph of the cross section of thin oxide scale and EDS element maps of 443 steel oxidised for 7200 s at 1150 °C in humid air.

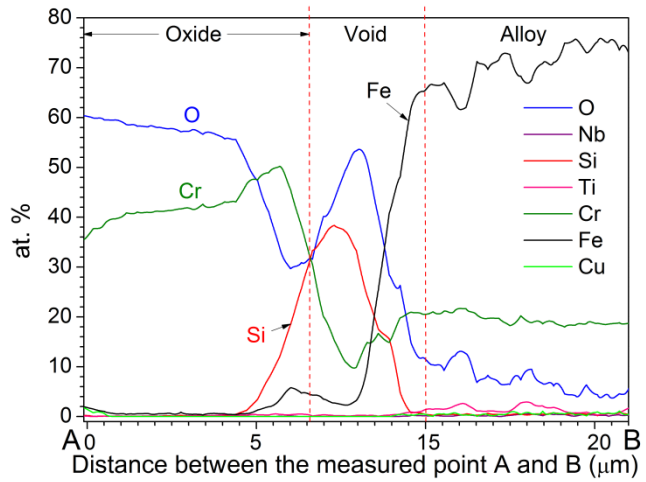

Fig. 9 The result of a EDS linescan along A-B in Fig.8b of thin oxide scale formed on 443 steel oxidised for 7200 s at 1150 °C in humid air. The oxide was a corundum structure M_2O_3 at the oxide/gas interface.

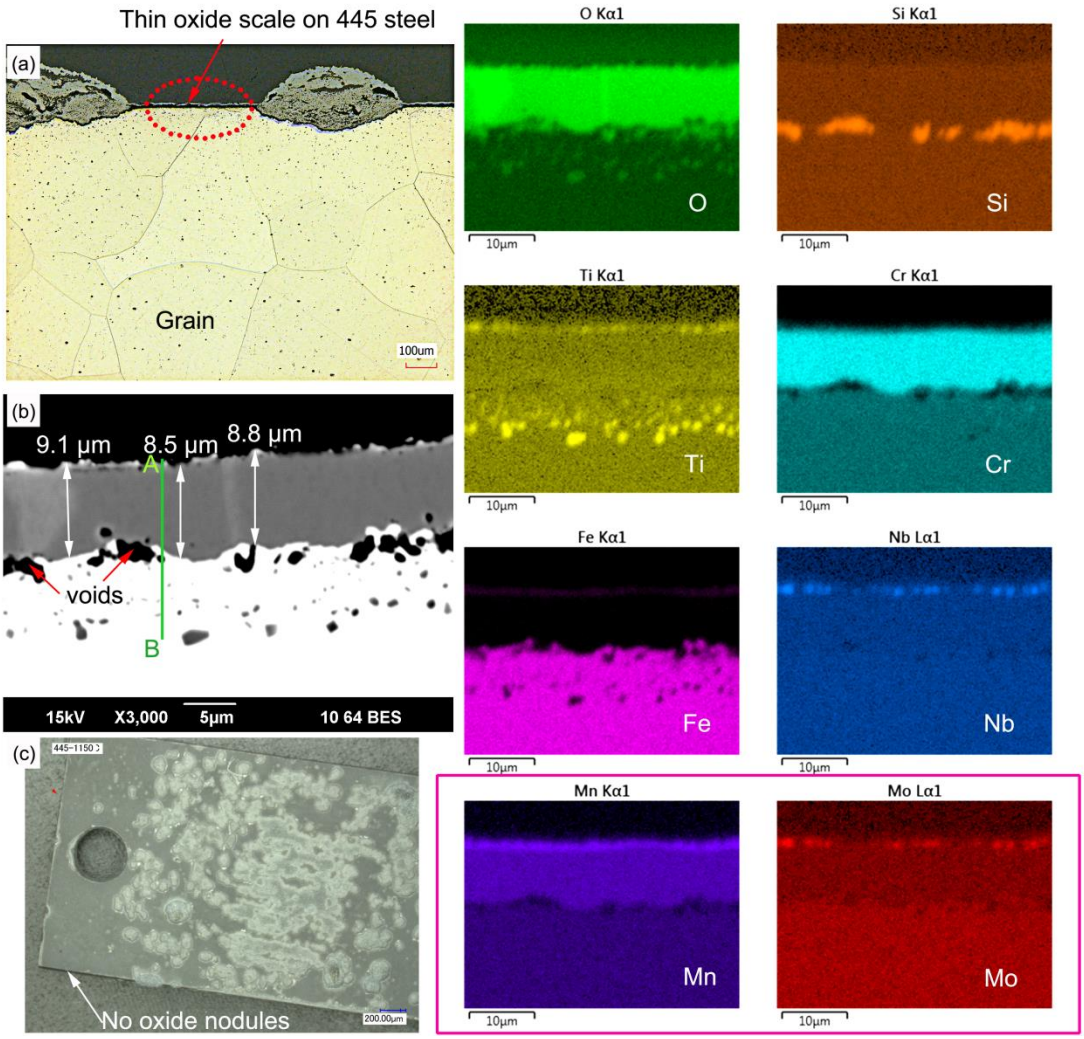

Fig. 10 (a) Optical micrograph of the cross section showing steel grains of oxidised 445 steel, (b) the BSE micrograph of the cross section of thin oxide scale and EDS element maps of 445 steel, and (c) image of oxidised surface of 445 steel oxidised for 7200 s at 1150 °C in humid air.

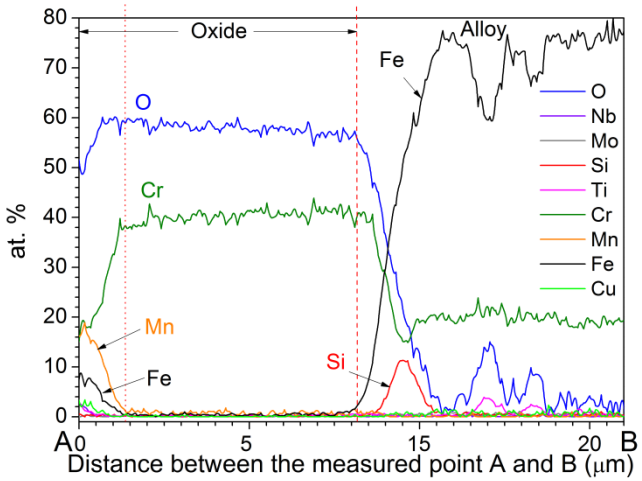

Fig. 11 The result of a EDS linescan along A-B in Fig.10b of the thin oxide scale formed on 445 steel oxidised for 7200 s at 1150 °C in humid air. The oxide was a spinel structure M_3O_4 at the oxide/gas interface.

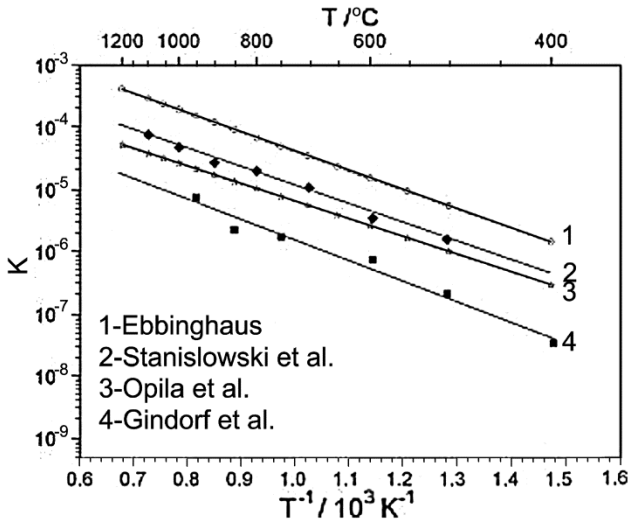

Fig. 12 Equilibrium constant K as a function of the inverse temperature for the reaction $1/2Cr_2O_3$ (s) + H_2O (g) + $3/4O_2$ (g) = CrO_2 $(OH)_2$ (g) according to in Ebbinghaus [48], Stanislowski et al. [49], Opila et al. [50], and Gindorf et al. [47]. Pure Cr_2O_3 was used for the reaction.